Topology of interacting coiled vortex rings

Robert M. Kerr †,

Department of Mathematics, University of Warwick, Coventry CV4 7AL, United Kingdom

(Received 4 August 2018)

Pairs of nested vortex rings, one with coils, are evolved numerically to compare their topological numbers to those of recent experiments (Scheeler *et al.* 2017). Included are the twist T, writhe Wr and self-linking $\mathcal{L}_S$ numbers, plus centreline helicities $\mathcal{H}_c$. The questions are: Can the experimental numbers be validated and do these numbers have roles in the dynamics of the global helicities $\mathcal{H}$ and enstrophies Z with respect to cascades? Topological analysis of the experiments $t = 0$ analytic centreline vortex trajectories validates only the writhe measurements, not their values of Tw and $\mathcal{L}_S$ which obey $Tw \lesssim \mathcal{L}_S = m \gg Wr$ for m-coil rings. Not $Tw \ll Wr$. To suggest why the large twists do not contribute to $\mathcal{H}$, it is noted that the mapping of the coiled rings onto the mesh is to a first approximation a single pair of Clebsch potentials, whose self-helicity $\mathcal{H}_S \equiv 0$. Numerical rings with circulations Γ, including some single rings, show small initial helicities with $\mathcal{H}(0) \approx \mathcal{H}_c \sim (1 \text{ to } 2)Wr\Gamma^2 \ll \mathcal{L}_S\Gamma^2$. For time and velocity scales that are consistent with the experiments, as the coils evolve their Tw, Wr, $\mathcal{L}_S$ numbers and their helicities are nearly static until reconnection. Nonetheless, Wr and Tw retain important complementary roles in the dynamics of the global helicity $\mathcal{H}$ and enstrophy Z, with the evolution of the torsion $\tau(s)$ profile showing the beginnings of a cascade to small scales.

1. Background

It has been known for over 100 years that two distinct nested and unlinked ideal vortex rings will leap-frog through one another as they propagate downstream with the inner ring becoming the outer ring and the outer ring becoming the inner.

How would this interaction be modified if the rings were coiled? Would the rings reconnect instead of leap-frogging and what diagnostics should be used? Scheeler *et al.* (2017) has recently shown how to experimentally generate coiled vortex rings and claim that they can follow the evolution of the rings' discrete topological properties. This includes their twist Tw, writhe Wr and self-linking $\mathcal{L}_S$ numbers (2.12), along with their centreline helicities $\mathcal{H}_{cj}$ (2.14). This could be an important advance and would provide evidence on the roles of topology, reconnection and helicity in the evolution of turbulence.

However, independent validation is required for the claim that their experiments can preserve the total helicity/self-linking $\mathcal{L}_S$, despite large transfers between Wr and Tw, and still satisfy

$$\mathcal{L}_S = Tw + Wr\,, \tag{1.1}$$

a constraint introduced by Calugareanu (1959) with a simplied proof by Pohl (1968). The concern is that only Wr and the $\mathcal{H}_{cj}$ are measured, with $\mathcal{L}_S$ obtained by assuming that $\mathcal{H} = \sum_j \mathcal{H}_{cj}$ and (1.2). Then (1.1) is used to find Tw, instead of being using to validate the Tw, Wr and $\mathcal{L}_S$ results.

A known test that immediately shows that one or more of their Tw, Wr and $\mathcal{L}_S$ results are incorrect is to independently determine all three numbers from the analytic closed

† Email address for correspondence: Robert.Kerr@warwick.ac.uk

trajectories (2.7) of Scheeler *et al.* (2017). This can be done using the algorithms of Moffatt & Ricca (1992) and shows that each topological number for the coil trajectories is positive with $Tw \gg Wr$, not $Tw \ll Wr$, raising questions about whether there is a physical role for the topological helicity:

$$\mathcal{H}_T = \sum_{i \neq j} \Gamma_i \Gamma_j \mathcal{L}_{ij} + \sum_j \Gamma_j^2 \mathcal{L}_{S_j} \tag{1.2}$$

where the Γ_j are the circulations of the vortices (2.10). Experimental and numerical trefoil vortex knots have found that during reconnection $\mathcal{H}_T$ is preserved, along with some exchange of linking between the writhe and twist (Scheeler *et al.* 2014; Kerr 2018a,b). However, the trefoils are a unique, extremely helical configuration. To determine whether the topological numbers consistently have roles in the dynamics of reconnection and the flow of turbulent energy to small scales, identifying those numbers correctly for less helical configurations such as coiled rings is essential.

Once the Tw, Wr and $\mathcal{L}_S$ discrepancies in the Scheeler *et al.* (2017) results were recognised, numerics were begun to help determine which of the inferred topological numbers are correct and what, if any, physical roles they might play. These numerical methods have previously been validated by comparisions with experiments, the reconnecting trefoil vortex knots of Kleckner & Irvine (2013), and used to obtain run-time values for Wr and $\mathcal{L}_S$ (Kerr 2018a). This paper complements those topological diagnostics with an improved algorithm for calculating the twist Tw (2.12) from the Frenet-Serret relations (2.11), one that is accurate enough to allow validation of all three topological numbers using (1.1).

The bottom line for the Scheeler *et al.* (2017) experimental topological numbers is that the new diagnostics and numerics confirm only the values of the $t = 0$ writhe Wr, and none of their reported Tw, $\mathcal{L}_S$ and $\mathcal{H}_c$ values. In particular, their claim that linking is exchanged between Wr and Tw with $Wr \gg Tw$ is not confirmed. In contrast, $Wr \ll Tw$, all the helicities are much smaller than the predictions of (1.2) and neither Wr nor Tw changes signficantly before reconnection ends.

Despite being static during reconnection, in this new picture the topological numbers Wr and Tw retain important complementary roles in the dynamics of the global helicity $\mathcal{H}$ (2.4) and enstrophy Z (2.3), dynamics that show the beginnings of a cascade to small scales. Specifically, it is Wr that controls the $\mathcal{H}_c$, and hence $\mathcal{H}$, values, not the self-linking $\mathcal{L}_S$, with

$$\mathcal{H} \approx \mathcal{H}_c \sim (1 \text{ to } 2) Wr \Gamma^2 \ll \mathcal{L}_S \Gamma^2 \,. \tag{1.3}$$

For the enstrophy Z, its growth in figure 6 could be tied to the development of small scales in the figure 3 s-profiles of the torsion $\tau(s)$, profiles whose s-integrals are the twist (2.12). The axial velocity profiles in 3 also provide clues to the surprisingly small experimental $\mathcal{H}_c$ in Scheeler *et al.* (2017), with values smaller than even those from (1.3).

The remainder of this paper is organised as follows. First, there is a summary of the underlying continuum equations, the diagnostics and the steps used to generate the numerical coiled rings. The results begin with single rings with single coils to illustrate the relationship between the linking and helicity diagnostics and the number and size of the coils. Then the time-evolving, nested two-ring cases are presented, with the focus upon cases with 5 coils on the inner ring because all of their topological diagnostics can be determined and validated and they have the cleanest $Z^{-1/2}$ enstrophy scaling. Besides comparing the experimental writhes Wr at $t = 0$, validation that these calculations represent the dynamics of the experimental coiled rings will come from the timescales over which the rings move in and about z and begin to swap positions. The temporal

evolution and scaling of the continuum helicity $\mathcal{H}$ and enstrophy Z are then related to how they behave in recent trefoil and anti-parallel reconnection calculations. Finally, how these numerical methods could determine the topological numbers of experimental vortices is noted.

2. Equations: continuum, initial states and diagnostics

The governing equations for the simulations are the incompressible Navier-Stokes equations in a periodic box with volume ($V = \ell^3$).

$$\left.\begin{aligned} \boldsymbol{u}_t - \nu\triangle\boldsymbol{u} + (\boldsymbol{u}\cdot\nabla)\boldsymbol{u} + \nabla p = 0 \\ \nabla\cdot\boldsymbol{u} = 0 \end{aligned}\right\} \quad \text{in } \mathbb{T}^3_\ell \times [0,T)\,. \tag{2.1}$$

The vorticity $\boldsymbol{\omega}(\boldsymbol{x}) = \nabla\times\boldsymbol{u}(\boldsymbol{x})$ equation is

$$\frac{\partial\boldsymbol{\omega}}{\partial t} + (\boldsymbol{u}\cdot\nabla)\boldsymbol{\omega} = (\boldsymbol{\omega}\cdot\nabla)\boldsymbol{u} + \nu\triangle\boldsymbol{\omega}, \qquad \nabla\cdot\boldsymbol{\omega} = 0\,. \tag{2.2}$$

The enstrophy density $|\boldsymbol{\omega}|^2$ equation and the volume-integrated enstrophy Z are

$$\frac{\partial|\boldsymbol{\omega}|^2}{\partial t} + (\boldsymbol{u}\cdot\nabla)|\boldsymbol{\omega}|^2 = \underbrace{2\boldsymbol{\omega}\boldsymbol{S}\boldsymbol{\omega}}_{Z_p=\text{production}} + \nu\triangle|\boldsymbol{\omega}|^2 - \underbrace{2\nu(\nabla\boldsymbol{\omega})^2}_{\epsilon_\omega=Z-\text{dissipation}}\,, \qquad Z = \int\boldsymbol{\omega}^2 dV\,, \tag{2.3}$$

where $\boldsymbol{S} = (1/2)(\nabla\boldsymbol{u} + \nabla\boldsymbol{u}^T)$ is the strain and the normalised enstrophy production rate or velocity-derivative-skewness is $-S_u = D\boldsymbol{\omega}\boldsymbol{S}\boldsymbol{\omega}/Z^{3/2}$. The helicity density h equation is

$$\frac{\partial h}{\partial t} + (\boldsymbol{u}\cdot\nabla)h = \underbrace{-\boldsymbol{\omega}\cdot\nabla\Pi}_{\omega-\text{transport}} + \underbrace{\nu\triangle h}_{\nu-\text{transport}} - \underbrace{2\nu\text{tr}(\nabla\boldsymbol{\omega}\cdot\nabla\boldsymbol{u}^T)}_{\epsilon_h=\mathcal{H}-\text{dissipation}} \qquad \mathcal{H} = \int\boldsymbol{u}\cdot\boldsymbol{\omega}dV\,. \tag{2.4}$$

where $\Pi = p - \frac{1}{2}\boldsymbol{u}^2 \neq p_h$, the pressure head $p_h = p + \frac{1}{2}\boldsymbol{u}^2$, amd $\mathcal{H}$ is the global helicity.

An alternative way to formulate incompressible velocity and vorticity fields is the Clebsch decomposition, which under Euler, can be defined by pairs of advected scalar fields $(a_j(\boldsymbol{x}), b_j(\boldsymbol{x}))$, for which the incompressible velocity and vorticity fields are

$$\boldsymbol{u} = \sum_j a_j\nabla b_j + \nabla\phi \quad \text{and} \quad \boldsymbol{\omega} = \sum_j \nabla b_j\times\nabla a_j\,. \tag{2.5}$$

where the extra $\phi(\boldsymbol{x})$ potential imposes incompressibility and whose $\boldsymbol{\omega}$ is similar to the definition of a pseudo-vorticity for a quantum fluid (Rorai *et al.* 2016). By applying integration by parts to the $\nabla\phi$ term one can show that the global self-helicity for a single pair (a_1, b_1) is identically zero:

$$\mathcal{H}_S = \int(\boldsymbol{u}_1\times\boldsymbol{\omega}_1)dV \equiv 0\,, \tag{2.6}$$

an identity that implies that at least two Clebsch pairs are required for there to be finite hydrodynamic helicity $\mathcal{H}$ and represents a fundamental difference between the magnetic helicity, defined as $\mathcal{H}_M = \int\boldsymbol{A}\cdot\boldsymbol{B}dV$ with $\nabla\cdot\boldsymbol{A}$ unspecified, and the $\nabla\cdot\boldsymbol{u}\equiv 0$ hydrodynamic helicity. Examples of configurations with finite helicity are linked rings, with each ring defined by its own Clebsch pair such that the helicity of their coupled velocities and vorticities is $2\mathcal{L}_{12}\Gamma_1\Gamma_2$. For the trefoil initialisation in Kerr (2018a), which gives $\mathcal{H}/\Gamma^2 \equiv \mathcal{L}_S = 3$, a second Clebsch pair should exist because two points from the trefoil were used to generate the vorticity at each mesh point. However, the coiled rings do not have an obvious second Clebsch pair, so (1.2) does not have to be obeyed.

Cases	$m_{\rm in}$	$m_{\rm out}$	A	Mesh	ν	Z_0	E_0	Tw_0	Wr_0	$\mathcal{L}_0$	$\mathcal{H}_0$
s_a	1	–	$\dagger_{25}$	256^3	$t=0$	5.14e5	1e8	0.67	0.33	1	$0.3\Gamma^2$
s_b	1	–	$\dagger_{50}$	256^3	$t=0$	6.8e5	1.31e8	0.29	0.71	1	$0.53\Gamma^2$
s_c	1	–	$\dagger_{100}$	256^3	$t=0$	5.14e5	1e8	0.83	-0.83	0	$-0.68\Gamma^2$
s_6	6	–	4.3	512^3	0.162	3.4e5	1.25e8	5.65	0.35	6	$0.36\Gamma^2$
c6o	0	6	4.3	256^3	0.162	1e6	6.6e8	5.81	0.16	6	$0.34\Gamma^2$
c5a	5	0	7	512^3	0.162	1.1e6	6.9e8	4.596	0.44	5	$0.76\Gamma^2$
c5b	5	0	7	1024^3	0.08	1.1e6	6.9e8	4.596	0.44	5	$0.75\Gamma^2$
c0	0	0	0	512^3	0.08	1.05e6	6.9e8	0	0	0	0
c9	9	0	4.3	512^3	0.162	1.11e6	6.8e8	7.62	1.36	(9 ± 1.5)	$1.5\Gamma^2$

TABLE 1. Viscosities and parameters for the initial conditions using (2.8). All the calculations were done in $(144\pi)^3 \approx 452^3$ domains with the radius of the inner (or only) ring in each case $R_{h\text{-in}} = 72$ and the outer ring $R_{h\text{-out}} = 120$. Mesh=the final computational mesh. For all the cases $a_0 = 18$ and $k_f = 84$ in (2.8), giving effective radii of $a_e = 21.6$, circulations of $\Gamma = 1720$, and $\omega_0 = 1.08$, except for c9 whose $\omega_0 = 1.14$ and whose $\mathcal{L}_S$ is uncertain, varying with $\Delta\mathcal{L}_S = \pm 1.5$ for $\delta = 0.09 \pm 0.025$ with $\varepsilon = 0.18$ in (2.13). The $t = 0$ global enstrophies Z_0, energies E_0 and helicities are given. For $\dagger_{25}$ the trajectory is $A(\phi) = 25\big((1-\sin\phi)^2 - (1-\sin\phi)\big)$ and for $\dagger_{50}$ and $\dagger_{100}$: $a(\phi) = a_f(1-\sin\phi)$ for a_f=50 and 100. For the $\nu = 0.16$ cases, the Reynolds number of $Re = \Gamma/\nu$=10,000 is comparable to the experimental values of Re=12,000-20,000.

2.1. *Summary of the calculations*

The initial trajectories of the coiled rings $\boldsymbol{X}_h(\phi) = \big(x, y, z\big)$ are:

$$\begin{array}{lll} x(\phi) = R(\phi)\cos(\phi) & y(\phi) = & R(\phi)\sin(\phi) \qquad z(\phi) = A(\phi)\cos(m\phi) \\ \text{where} & R(\phi) = & R_h + A(\phi)\sin(m\phi) \quad \text{with } \phi = [1 : 2\pi]\,. \end{array} \tag{2.7}$$

For all the $m \neq 1$ cases, R_h, and $A(\phi)$ are the values used by Scheeler *et al.* (2017).

Once all the trajectories are defined, vortices of finite radii are mapped onto the mesh (Kerr 2013). First, a preliminary field of two superposed vortex rings $\boldsymbol{\omega}_j(\boldsymbol{x})$, $j \in [1, 2]$, is generated using the Rosenhead regularisation of a point vortex (2.8) with radii of a_0, multiplied by the tangent $\boldsymbol{T}_j(\phi)$ (2.11) at $\boldsymbol{x}_j(\phi)$: $\boldsymbol{\omega}_j(\boldsymbol{x}_j) = |\omega_j(\boldsymbol{x}_j)|\boldsymbol{T}_j(\phi)$, where $r = |\boldsymbol{x} - \boldsymbol{x}_j(\phi)|$ and $\boldsymbol{x}_j(\phi)$ is the nearest point on the coiled ring. This and the next step use

$$|\omega_j|(\boldsymbol{x}) = \Gamma\frac{(a_0^2)}{(r^2+a_0^2)^2}, \quad \tilde{\boldsymbol{\omega}}_f(\boldsymbol{k}) = \tilde{\boldsymbol{\omega}}_i(\boldsymbol{k})\exp\left(-\frac{k^4}{k_f^4}\right) \quad \text{and} \quad a_e = \left(\frac{\Gamma}{\omega_0\pi}\right)^{1/2}, \tag{2.8}$$

where the k_f hyperviscous smoothing is applied to the preliminary Fourier transformed $\tilde{\boldsymbol{\omega}}_i(\boldsymbol{k})$ field to get $\tilde{\boldsymbol{\omega}}_f(\boldsymbol{k})$. Incompressibility is then applied before the Fourier fields are transformed back to give a final $\boldsymbol{u}(\boldsymbol{x})|_{t=0}$ field. The vortices of the initial coiled rings all have a circulation of $\Gamma = 1720$ and after the smoothing, their effective radii have increased to $a_e \approx 1.2a_0 = 21.6$, with their initial peak vorticities adjusted to be $\omega_0 \approx 1$

The initial conditions, including the initial twist Tw_0, writhe Wr_0 and global helicities $\mathcal{H}_0$, for all of the simulations are given in table 1. The single ring cases demonstrate the range of Tw and writhe Wr generated by different trajectories and how they contribute to the continuum helicities $\mathcal{H}$. The multi-coil cases are a single ring with 6 coils, a nested pair with a 6 coil outer ring and two nested pairs with inner ring coils, one with 5 coils and one with 9. The centreline trajectories of the 6 and 9 coil cases are given by the experimental hydrofoils (Scheeler *et al.* 2017). The rings are visualised using vorticity isosurfaces and centreline vortices within those isosurfaces in figures 1, 2a and 4a

Validation that the computational coiled vortices represent the new ring experiments

is done in two ways. One is the values of the $t = 0$ writhe. The other validation is, as in Kerr (2018a), to scale the rings' evolution by the nonlinear time and velocity scales,

$$t_\Gamma = R_e^2/\Gamma \quad \text{and} \quad U_z \sim \Gamma/R_e\,, \tag{2.9}$$

where R_e is the average radii of the vortex rings. This allows comparisons between the times that the numerical and experimental rings pass one another and how far the rings have propagated by those times.

The calculations use the same filtered pseudospectral method (Kerr 2013) as the trefoil calculations, with that experience used to guide the choice of ν for the given ratios of the vortex thicknesses to the resolution. The one proper resolution test is cases c5a,b, which were run on both 512^3 and 1024^3 meshes, at different viscosities, ν=0.162 and 0.08, for which the small increases in $\|\omega\|_\infty$ as ν decreased and resolution improved were consistent with those observed at early times in Kerr (2018b).

2.2. *Vortex line diagnostics*

Once the three-dimensional simulations have been run, for the two $j \in [1, 2]$ vortex rings, one coiled, the positions $\boldsymbol{x}_j(s_j, t)$ of their centreline vortices can be identified by applying the stream3 function in Matlab to seed-points $\boldsymbol{x}_j(s = 0)$ at, or near, local vorticity maxima:

$$\frac{d\boldsymbol{x}_j(s)}{ds} = \boldsymbol{\omega}(\boldsymbol{x}_j(s)) \quad \text{with circulations given by} \quad \Gamma_j = \oint_{\mathcal{D}_j} \boldsymbol{u}_j \cdot d\boldsymbol{r}_j\,, \tag{2.10}$$

where the $\boldsymbol{r}_j \in \mathcal{D}_j$ are taken about the $\boldsymbol{x}_j(s)$. The $\boldsymbol{x}_j(s)$ curves, which tend to have thousands of points, rarely close exactly upon themselves. To get closed curves, stream3 is run in opposite directions from the local ω maxima, giving curves that nearly meet on the opposite side of the rings from their $\boldsymbol{x}_j(s{=}0)$. These are then linearly blended using 128 points on either side of where they nearly meet to produce closed rings.

Given there are closed curves, the topological numbers Tw, Wr and $\mathcal{L}_S$ can, in principle, be found using the Frenet-Serret relations

$$\boldsymbol{T}_j = \partial_s \boldsymbol{x}_j/|\partial_s \boldsymbol{x}_j|; \quad \kappa \boldsymbol{N}_j = \partial_s \boldsymbol{T}_j; \quad \tau \boldsymbol{B}_j - \kappa \boldsymbol{T}_j = \partial_s \boldsymbol{N}; \quad \tau \boldsymbol{N}_j = -\partial_s \boldsymbol{B}_j\,; \tag{2.11}$$

for which the twist given in principle by

$$Tw_j = \frac{1}{2\pi} \oint \tau ds, \qquad \text{using} \quad \tau = \frac{d\boldsymbol{N}}{ds} \cdot \boldsymbol{B} \tag{2.12}$$

with $\mathcal{L}_{Sj}$ and Wr_j determined by regularised Gauss linking integrals between loops

$$\mathcal{L}_{jk} = \sum_{jk} \frac{1}{4\pi} \oint_{\mathcal{C}_j} \oint_{\mathcal{C}_k} \frac{(d\boldsymbol{x}_j \times d\boldsymbol{x}_k) \cdot (\boldsymbol{x}_j - \boldsymbol{x}_k)}{(|\boldsymbol{x}_j - \boldsymbol{x}_k|^2 + \delta^2)^{1.5}} \quad \text{with} \quad \boldsymbol{x}_k = \boldsymbol{x}_j + \varepsilon \boldsymbol{N}_j\,. \tag{2.13}$$

That is, $\mathcal{L}_{Sj}$ can be got by defining $\boldsymbol{x}_k$ as an $\varepsilon \boldsymbol{N}_j$ push added to $\boldsymbol{x}_j$, then applying (2.13). Or $\boldsymbol{x}_k$ could come from a slightly different seed in (2.10). To get the writhe Wr one uses $k{=}j$ and $\delta \neq 0$ in (2.13). These steps are based upon the suggestions of Berger & Field (1984), then applied to analytic curves by Moffatt & Ricca (1992).

To obtain consistent Wr and $\mathcal{L}_S$, some care is required in the choice of the two small parameters, δ and ε. If δ and ε are too small, the kernel of (2.13) can become very large, and if δ and ε are too large, the original coiled ring is not being represented. For all of the time-evolving cases in table 1, except c9, the $\mathcal{L}_S$ did not vary by more than 0.05 as ε is varied by a factor of 4 and the Wr varied by only a few percent as δ was changed by a factor of 20.

This leaves as undetermined only the torsion τ and the twist Tw, the integral of τ (2.12). Previously, Rorai *et al.* (2016) applied Frenet-Serret (2.11) to time-evolving quantum pseudo-vorticity lines to find their curvature κ and normal vectors $\boldsymbol{N}$. However, calculating the torsion $\tau(s)$ requires a third-derivative of the trajectory positions, leading to the problem illustrated by figure 3 for the centreline trajectory $\boldsymbol{x}_{\rm in}(s_{\rm in})$ of the inner coiled ring of c5. What is plotted first is $\tau_1(s)$, where the subscript 1 indicates that this $\tau(s)$ solution uses every point of $\boldsymbol{x}_{\rm in}$. This curve has strong oscillations that are due to the high-frequency flutter generated by the ODE45 function contained within Matlab's stream3 solutions for $\boldsymbol{x}_{\rm in}(s_{\rm in})$. Flutter that is amplified by the third-derivatives that determine $\tau_1(s)$.

Despite these oscillations, the $\tau_1(s)$ stay within a clear envelope, so applying (2.12) to $\tau_1(s)$ still gives Tw values that are close to expectations. Could a simple smoothing or interpolation of the points in the $\boldsymbol{x}_j(s)$ suppress the oscillations and improve the results? Only one method has worked: Using only every fourth point on the trajectories to find $\tau_4(s_{\rm in})$ from $\boldsymbol{x}_{\rm in}(s_{\rm in})$.

Taken together, these algorithms provide independent determinations of Tw, Wr and $\mathcal{L}_S$ for which $Tw+Wr$ and $\mathcal{L}_S$ do not vary from their expected m-integer values by more than 0.02 and 0.05 respectively. This provides validation by the (1.1) constraint until the first reconnection finishes, with the exception in table 1 being $\mathcal{L}_S$ for c9 due to its tightly wound coils.

What, if any, relationship is there between these topological numbers and the global helicity $\mathcal{H}$? Moffatt & Ricca (1992) suggested (1.2), with only $\mathcal{L}_S$ having a role. Scheeler *et al.* (2017) suggests taking an intermediate step, using centreline helicities $\mathcal{H}_{cj}$ as proxies for the $\mathcal{H}$ where

$$\mathcal{H}_{cj} = \Gamma_j \oint_{\mathcal{C}_j} \boldsymbol{u}_j \cdot d\boldsymbol{x}_j = \quad \Gamma_j \oint_{\mathcal{C}_j} u_\omega(s) |\partial \boldsymbol{x}_j/\partial s| ds, \quad u_\omega = \boldsymbol{u}_j \cdot \boldsymbol{T}_j \,, \tag{2.14}$$

with the circulations Γ_j determined using (2.10). Note that both the $\mathcal{H}_{cj}$ and the Γ_j (2.10) in Scheeler *et al.* (2017) are found using closed velocity path-integrals, with the experimental velocities determined using PIV, particle-image-velocimetry.

This is the first time circulations have been measured instead of being estimated by either a flat-plate approximation (Kleckner & Irvine 2013) or with a correction due to camber (Kerr 2018a), which are respectively

$$\Gamma_{\rm fp} = \pi U C \sin(\theta) \quad \text{and} \quad \Gamma = \Gamma_{\rm fp} + \Delta\Gamma_{\rm cam} \approx 1.5 \Gamma_{\rm fp} \,. \tag{2.15}$$

Do the measured coiled ring circulations of Scheeler *et al.* (2017) correspond to either prediction? Surprisingly, neither is correct. Instead, by applying values from the Scheeler *et al.* (2017) supplement to these predictions, with $U = 1.75$m/s the speed of their model, $C = 15$mm the chord (or width) of the hydrofoil ribbons and $\theta = 35°$=0.61rad the angle of attack, the measured circulation is $\Gamma \sim UC$, a factor of 1.8 less than the $\Gamma_{\rm fp}$ prediction. Nonetheless, using the times t_q when $r_{in} \approx r_{out}$ in figures 2a and 4a, respectively $t_q = 7.5$ and 10.5, and scaling them by $t_\Gamma = 5.35$ (2.9), one gets t_q/t_Γ=1.4 and 1.95 respectively.

To compare to the experimental times, scaling using t/t_Γ (2.9) is needed. To get there, what are given in Scheeler *et al.* (2017) are $t^* = (\nu/a_0^2)t$, where $a_0 = 1.5$mm and $\nu/a_0^2 = 0.44$, with the structural evolution shown in the on-line S2 and S3 experimental movies. Using $t_q^* - t_0^* \approx 0.3$ as the equivalent times for when the rings swap positions and the empirical circulation $\Gamma = UC$ to get t_Γ (2.9), after removing the ν/a_0^2 scaling on t one gets experimental $t_q/t_\Gamma \approx 2$, which is qualitatively similar to t_q/t_Γ=1.4 and 1.95 for numerical cases c5a,b and c6o.

The second set of closed velocity integrals are those taken along vortex lines to get

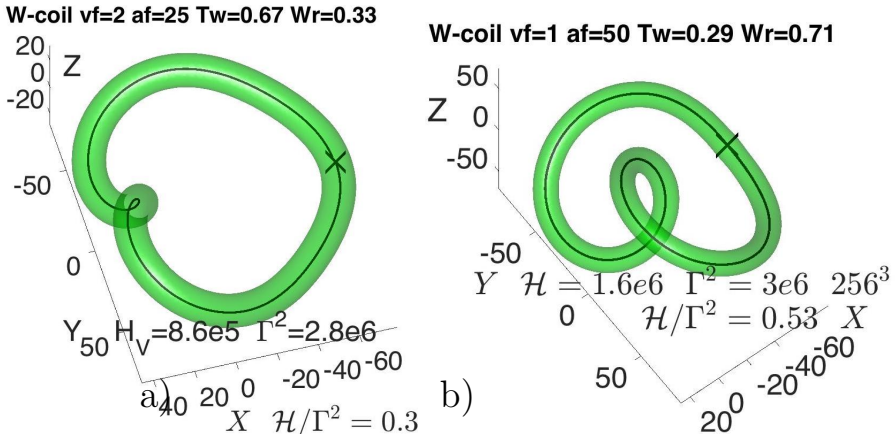

FIGURE 1. Two single rings with a single coil. a) Case s_a has a smaller coil and is twist-dominated with $Tw = 0.67$, $Wr = 0.33$ and $\mathcal{L}_S = 1$, like all the multi-coiled rings used for the nested ring calculations. b) Case s_b has a single mid-sized, writhe-dominated coil with $Tw = 0.29$, $Wr = 0.71$ and $\mathcal{L}_S = 1$.

$\mathcal{H}_c$ (2.14). Analysis shows that numerically $\sum_j \mathcal{H}_{cj}$ is a good proxy for $\mathcal{H}$ until the first reconnection ends, as reported in the Scheeler *et al.* (2017) supplement. However, each of the Scheeler *et al.* (2017) experimental values of $\mathcal{H}_c/\Gamma^2$ are approximately 1/3 the $t = 0$ numerical values in table 1. This is discussed below using figure 3.

3. Results

The results are broken into four parts. First analysis of single ring initial states that demonstrate that the twists Tw of all the analytic trajectories with small coils are large, with $Tw \lesssim \mathcal{L}_S \sim m$ the number of coils of the rings, and small writhes $Wr \lesssim 1$. Then, after mapping the trajectories onto the mesh, the relationships between the linking numbers and the continuum helicities are found. After the single-ring diagnostics clarify these relationships, the methods are applied to the interaction and reconnection of nested rings, inner coiled then outer coiled, and last, the evolution of the global diagnostics is presented.

3.1. *Single rings, single coil*

Figure 1 shows two single ring/single coil initial conditions to demonstrate what the topological twist and writhe are physically and provide comparisons to the illustrations that Scheeler *et al.* (2017) called the twist and writhe of vortices. In those illustrations, twist is represented as a bundle of swirling vortices about a common axis, a property of systems with an internal structure, for example DNA, but a property that does not exist for vortices in a continuum fluid.

For the vortices considered in this paper, both experimental and numerical, the only relevant topological properties are those given in table 1 for the centreline vortices and the continuum. Twist is illustrated in figure 1a using a single ring with a single, small coil that has $Tw = 0.67$, $Wr = 0.33$ and $\mathcal{L}_S = m = 1$. All of the multi-coil rings whose trajectories follow (2.7) are similar in that their twist is $Tw \lesssim \mathcal{L}_S \lesssim m$ and $Wr \lesssim 1$.

Figure 1b illustrates writhe using a ring with a modest coil, for which $Tw = 0.3$, writhe is $Wr = 0.67$ and $\mathcal{L}_S = m = 1$. While this is similar to the illustration of writhe in Scheeler *et al.* (2017), figure 1b does not represent the coiled experimental rings (2.7), whose coils are smaller and are a closer match to 1a.

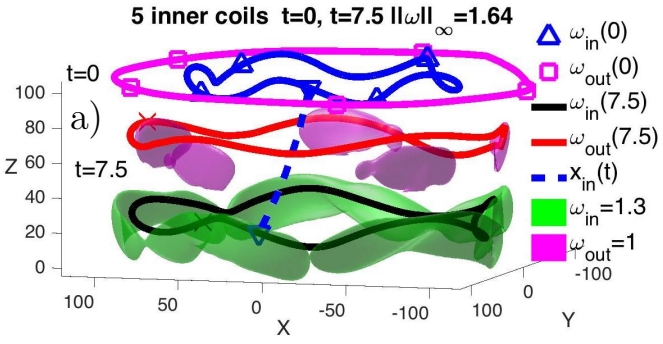

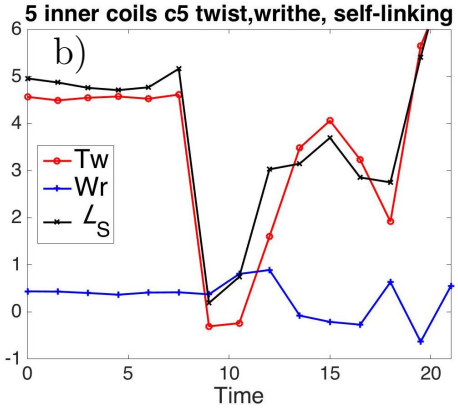

FIGURE 2. a) Visualisation of case c5, two rings whose inner ring has 5 coils. The $t = 0$ centreline vortices are indicated at the top by the curves with □ and △ symbols. Centreline vortices passing through two isosurfaces at $t = 7.5$ show the configuration as reconnection ends. The blue–dashed curve indicates the Lagrangian motion $\boldsymbol{x}_{\rm in}(s_c, t)$ of a point (s_c) on one of the inner coils whose velocity (3.1) is $(u_{\phi\text{-in}}, u_{z\text{-in}})$ ≈(10.3,-10.9) as it moves to the outside of the magenta uncoiled ring.

2b) Evolution of Tw, Wr and $\mathcal{L}_S \sim Tw(t)$, which are all relatively constant until the rings interact, partially reconnect and swap positions at $t_q \approx 7.5$. To compare to the experimental times, scaling using (2.9) gives $t_q/t_\Gamma \approx 1.4$ for case c5a, with the experimental timescales given after (2.15).

What are the helicities, centreline $\mathcal{H}_c$ and global $\mathcal{H}$ (2.14) generated by these single rings with coils? Earlier trefoil calculations found that $\mathcal{H} = \mathcal{H}_T$ is obeyed for trefoils (Kerr 2018a,b). For the two cases in figure 1, plus two others in table 1, to an order of magnitude $\mathcal{H}_c \approx |Wr|\Gamma^2$ (1.3), consistent with a Laing *et al.* (2015) suggestion that the twist might only be of secondary importance in determining $\mathcal{H}$. This writhe dependence even holds for case s_c, a single massive coil version of case s_b in figure 1 with $Wr \approx -Tw$ and $\mathcal{L}_S \approx 0$. One way to interpret the small coil result is that the intermediate vorticity field $\boldsymbol{\omega}_i(\boldsymbol{x})$ (2.8) is nearly a single Clebsch pair (2.5), whose self-helicity is identically zero, $\mathcal{H}_S \equiv 0$ (2.6).

3.2. *Two rings, inner coiled*

The primary cases for comparison with the experiments are the nested rings, with one coiled and the other uncoiled. These are c6o with a 6 coil outer ring in figure 4, cases c5a,b with a 5 coil inner ring in figures 2 and 3 and case c9 with a 9 coil inner ring. In the three-dimensional images, the original $t = 0$ outer and inner rings at the top are indicated by magenta and blue centreline vortices respectfully and at the later reconnection times, magenta and green isosurfaces indicate how those rings have evolved.

The centrelines of c6o and c9 are exactly those from the experiments, but because the c9 coils were too tight to allow consistent determination of its self-linking $\mathcal{L}_S$, the c5a,b cases were run to provide an inner coiled case for which all the topological numbers could be found. This allows validation using (1.1) and for this reason the c5 cases are used for most of the global analysis in figure 5.

The following is observed for all the nested rings. Their global helicities $\mathcal{H}$ in figure

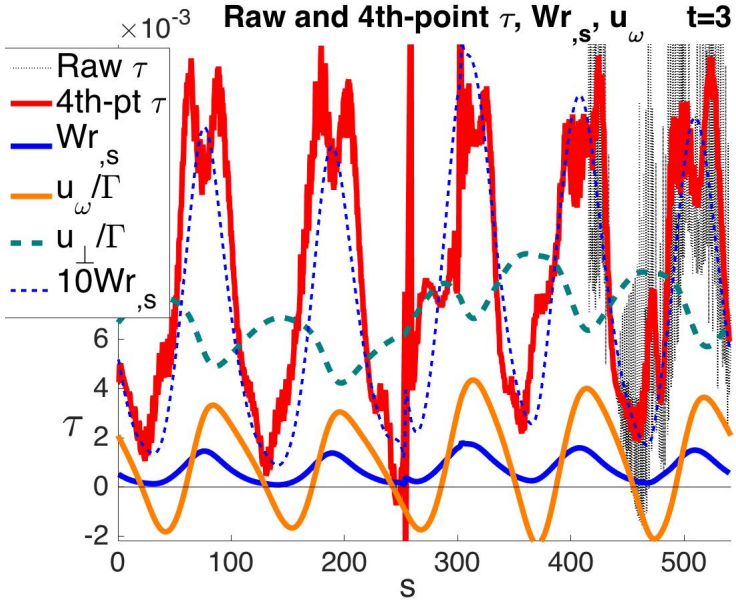

FIGURE 3. For case c5a, profiles of the torsion τ (2.11), gradient of the writhe $Wr_{,s}$, and weighted velocities u_ω/Γ and $u_\perp/\Gamma = |\boldsymbol{u} - u_\omega \boldsymbol{T}|/\Gamma$. τ is calculated using only every 4th point (red) to control the large fluctuations generated by the raw data (black with only $s > 400$ shown). $10Wr_{,s}$ follows τ, but the u_ω/Γ that contribute to $\mathcal{H}_c$ (2.14) have stronger variations, including $u_\omega/\Gamma < 0$. $\mathcal{H}_c/(\Gamma^2 Wr) = \int ds\, u_\omega/(\Gamma Wr) = 1.4 > 1$, similar to $\mathcal{H}/Wr\Gamma^2$ in figure 5. The perpendicular velocities on the trajectories $u_\perp/\Gamma$ are the order of $|U_z|$.

5 are preserved until at least $t = 6$ and all have similar enstrophy growth, with the strongest for case c5b. For their topological numbers, the self-linking identity (1.1) is satisfied at all cases either by direct determination of Wr, Tw and $\mathcal{L}_S$, or for case c9 by assuming that $\mathcal{L}_S = m = 9$. There are also almost no changes in these numbers until reconnection, including no exchange of $\mathcal{L}_S$ between between the twist and the writhe.

Figure 2 shows how the structure and topological numbers for case c5a evolve. In 2a, the $t = 0$ centreline vortices are at the top and the $t = 7.5$ structures are at the bottom, with the beginning of reconnection represented by the magenta bulges on the previously outer ring that contain helicity that has been transferred from the inner to the outer ring during reconnection.

Figure 2b shows that the topological numbers on that inner, coiled ring are relatively static for $t \leqslant 7.5$ with $\mathcal{L}_S = m = 5$, $Tw \lesssim 5$ and the writhe $Wr \approx 0.44$. While twist does not become writhe, as reported experimentally in figure 3 Scheeler *et al.* (2017), their $\tau(s)$ profiles do deform, with the $\tau(s)$ peaks splitting, beginning with those shown at $t = 3$ in 3. Post-reconnection, some of the original inner-coil, self-linking re-emerges at $t \geqslant 10.5$ with different topological numbers. There is a reduction of $\mathcal{L}_{S,\text{in}}$ on the original coiled ring along with new, self-linking of $\mathcal{L}_{S,\text{out}} = 1$ on the original outer ring from the $t = 7.5$ magenta bulges. The net change in the global linking is $\Delta\mathcal{L}_T \approx -1$ or using (1.2), $\Delta\mathcal{H}_T \approx -\Gamma^2$.

The dashes in figures 2a and 4a show the azimuthal+vertical motion of the coils, motion that could be compared to experimental measurements. Quantitatively,

$$\boldsymbol{u}_{\text{in}} = \dot{\boldsymbol{x}}_{\text{in}}(s,t) = (u_{\phi\text{-in}}\hat{\boldsymbol{e}}_\phi, u_{z\text{-in}}), \quad \text{and} \quad \boldsymbol{u}_{\text{out}} = \dot{\boldsymbol{x}}_{\text{out}}(s,t) = (u_{\phi\text{-out}}\hat{\boldsymbol{e}}_\phi, u_{z\text{-out}})\,. \tag{3.1}$$

The two $t = 3$ components of $\boldsymbol{u}_\perp = \boldsymbol{u} - u_\omega \boldsymbol{T}$, first averaged over the c5 inner ring, then

for U_z averaged over both rings, are

$$\overline{u}_{z\text{-in}} = 10.9\,, \quad \overline{u}_{\phi\text{-in}} \approx \overline{(u_\perp - \overline{u}_{z\text{-in}})} = 10.3 \quad \text{and} \quad U_z = 0.5(\overline{u_{z\text{-in}}} + \overline{u_{z\text{-out}}}) = 6.8\,, \tag{3.2}$$

consistent with the (2.9) prediction. The experimental case c9 has similar values, except with more coils its $\overline{u}_\phi$ is larger.

Using these velocities, figure 3 includes s-profiles at $t=3$ of u_ω/Γ and $u_\perp/\Gamma$ in addition to $Wr_{,s}$ in order to gain insight into the relationship between $\mathcal{H}_c$ (2.14), an integral of u_ω, and $Wr_{,s}$ in the simulations. As well as insight into why the $\mathcal{H}_c$ from the Scheeler *et al.* (2017) experiments are unexpectedly small. These insights are:

First, consider the small $t = 0$ values of Wr and $\mathcal{H}_c$ in table 1, with $\mathcal{H}_c/\Gamma^2 \sim 0.15Tw$, which is significantly less than the (1.2) prediction that $\mathcal{H}_T/\Gamma^2 \sim \mathcal{L}_S \sim Tw$. Second, u_ω has extensive negative excursions, $u_\omega \lesssim 0$. These negative excursions and small averages could make their line integral, $\mathcal{H}_c$, difficult to determine experimentally given their acknowledged difficulties in measuring the centreline velocities and could explain why theit $t=0$ experimental helicities, their *total* $\mathcal{H}_s$, are consistently $\approx 1/3$ of $Wr\Gamma^2$, compared to the equivalent simulations: Cases s6, c6o and c9. Could this be due to a consistent π^{-1} bug in their analysis? Or can this effect be reproduced in the simulations?

Surprisingly, it seems likely that the two stages in the analysis of case c9 could be reproducing this effect. In the first stage, when every point on the trajectory was used to calculate the topological numbers, besides the difficulties noted in table 1 with $\mathcal{L}_S$ for c9, the c9 writhe was $Wr_1 \approx 0.85$, such that $Tw_1 + Wr_1 \approx 8.4 < m = 9$ and $\mathcal{H}_c$ was about half the global helicity $\mathcal{H}$. However, with the 4th-point algorithm, for the values in table 1, $Tw_4 + Wr_4 \approx 9 = m$. Since it is writhe more than twist that is tied to $\mathcal{H}_c$ (2.14), this could be an example of how large fluctuations in the centreline velocities could lead to underestimates of $\mathcal{H}_c$.

3.3. *Two rings, outer coiled*

Figure 4 gives the structures and topological numbers of case c6o, with 6 coils on the outer ring. Before $t = 10.5$, on the coiled ring $\mathcal{L}_S = m = 6$, $Tw \lesssim 6$ and the writhe is small, $Wr \approx 0.16$. At $t = 11.25$, $\mathcal{L}_S$ and Tw jump to ≈ 0, then briefly rebound to approximately $\mathcal{L}_S = 6 \gtrsim Tw$ for $t \geqslant 13.5$, before the rings merge at $t \approx 15$. Throughout the calculation, the global $\|\omega\|_\infty$ stays on the black vortex line running through the inner, uncoiled ring, plateauing at $\|\omega\|_\infty \approx 2$ at $t \approx 10.5$, smaller than for case c5, while the local max $|\omega|$ on the outer coiled ring barely changes.

3.4. *Time dependencies of global $\mathcal{H}$ and vorticity statistics.*

The evolution of the continuum helicity $\mathcal{H}$ (2.14) and the enstrophy Z (2.3) given in figures 5 and 6 allows comparisons to be made between the reconnecting coiled rings and the reconnection of trefoil vortex knots and anti-parallel vortices in Kerr (2018a,b).

First the similarities between the two-ring configurations. By weighting $\mathcal{H}$ by $Wr\Gamma^2$, figure 5 shows that $\mathcal{H} \sim$(1 to 2)$Wr\Gamma^2$ until there is reconnection, already indicated by the sudden changes in Tw and $\mathcal{L}_S$ in figures 2b and 4b for $t \sim 7.5$ and 10.5 respectively. One difference between the inner and outer coiled ring cases is that post-reconnection, $\mathcal{H}/Wr\Gamma^2$ decreases for the inner coiled cases (c5a,b, c9) and increases for the outer coiled case (c6o). For the trefoils, reconnection is also associated with when $\mathcal{H}$ begins to change (Kerr 2018a).

For the enstrophy Z, as it grows, $Z^{-1/2}$ decreases linearly for all the nested, coiled cases during the first temporal stage, defined by relatively constant $\mathcal{H}$ up to $t \approx 7.5$ to ≈ 11 depending on the case. This scaling improves slightly between cases c5a and c5b as ν decreases. If there are no coils, case c0, enstrophy growth comes only from the two-ring

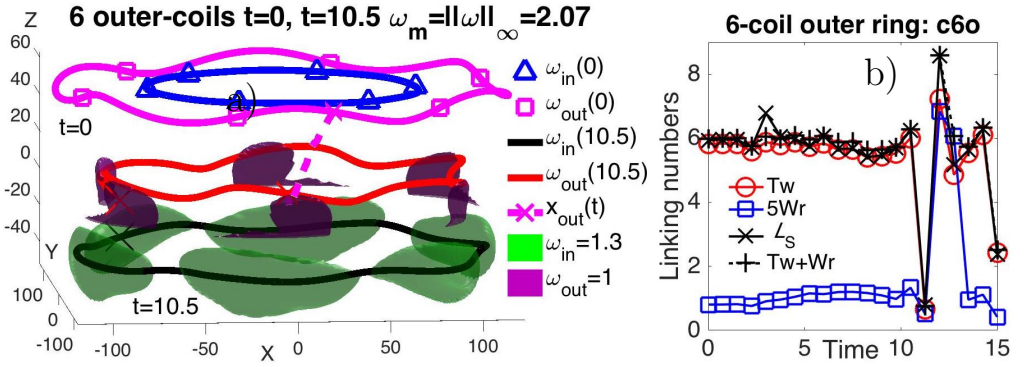

FIGURE 4. c6o, with a 6 coil outer ring. a) At the top are $t = 0$ centreline vortices ($\square, \triangle$) and at the bottom are $t_q = 10.5$ isosurfaces with centreline vortices that show the configuration as reconnection ends. Dashes show the $\boldsymbol{x}_{\rm out}(s_c, t)$ motion (3.1) of an outer coil (s_c) as that ring moves inside the $t=0$ uncoiled ring. b) Evolution of Tw, Wr and $\mathcal{L}_S$, which are almost constant until the rings interact and partially reconnect at $t_q \approx 10.5$ when they swap positions in a). The scaled reconnection/swapping time is $t_q/t_\Gamma \approx 1.95$ (2.9).

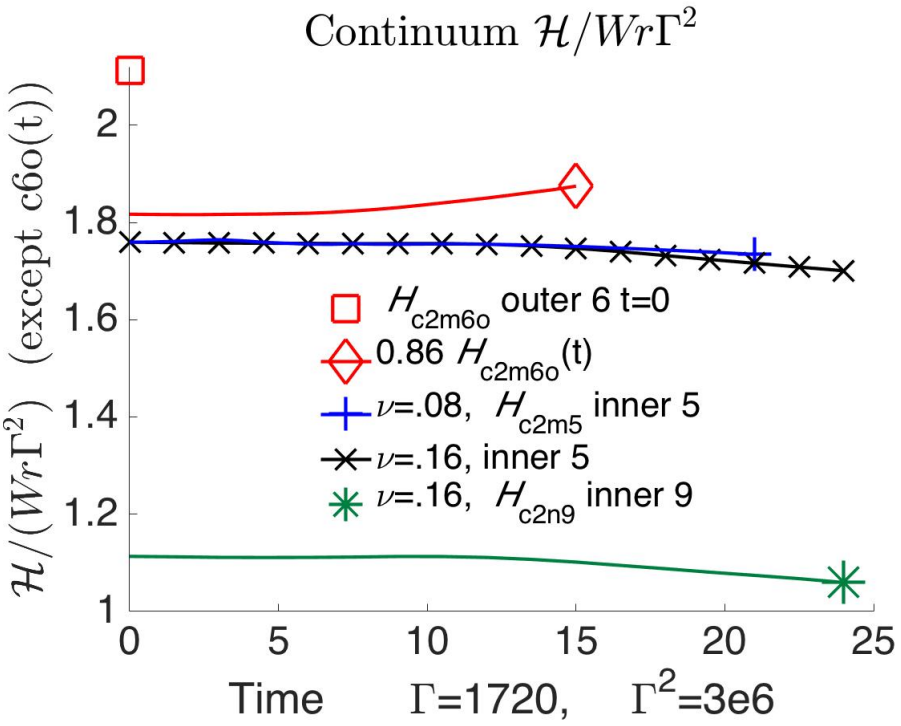

FIGURE 5. Continuum helicities normalised by $Wr\Gamma^2$ for two rings with one coiled. For inner rings with $m = 5$ and 9 coils, $\mathcal{H}(0) \approx (1.8 \text{ and } 1.1)Wr\Gamma^2$ until $t \approx 12$, twice the reconnection time of $t \approx 7.5$ indicated by jumps in the topological numbers in figure 2b. For an outer ring with 6 coils, $Wr \approx 0.16$ is small with $\mathcal{H}(0) \approx 2.1Wr\Gamma^2$ until reconnection ends, then $\mathcal{H}$ grows.

leap-frog interaction and if there is only one multi-coil ring, case s_6, from the relaxation of the coils, suggesting that the linear in time $Z^{-1/2}$ scaling requires both coils and nesting.

Is the $Z^{-1/2}$ scaling for nested coiled rings viscous or inviscid? Consider the insets in figure 6, with $\|\omega\|_\infty$, the maximum of vorticity, in the upper-right and $-S_u = C\boldsymbol{\omega}\boldsymbol{S}\boldsymbol{\omega}/Z^{3/2}$,

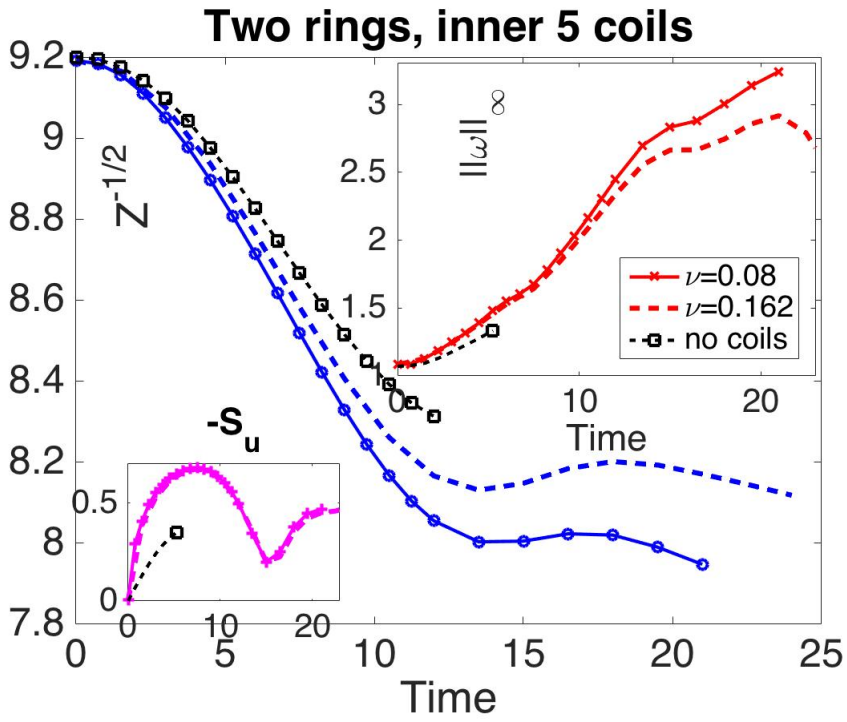

FIGURE 6. As the enstrophy Z grows, $Z^{-1/2}$ decreases linearly for c5a,b until $t \approx 11$, when reconnection finishes (when $\mathcal{L}_S$ rebounds in figure 2b) and helicity starts changing. c6o and c9 have similar $Z(t)^{-1/2}$. The enstrophy growth is weaker for s_6, a single ring with coils, and c0, nested rings with no coils, In the upper inset, $\|\omega\|_\infty$ has similar case-dependent growth. In the lower inset, the normalised enstrophy production $-S_u$ (2.3) is large for the 5 coil cases, independent of ν, and very weak for cases c0 (shown) and s_6.

the normalised enstrophy production (2.3) or velocity-derivative-skewness, in the lower-left. Both are independent of ν until about $t = 6$, implying that the calculations are essential inviscid, or Euler, until then. And given that, then the enstrophy growth can be understood in terms of the variations in $-S_u$. As $-S_u$ is increasing strongly for $t \leqslant 3$, Z does not change significantly. Then as the inner ring is pulled outside of the outer ring, $-S_u$ is relatively constant, allowing use of the classic closure of $dZ/dt = C_Z|S_u|Z^{3/2}$, which gives the observed linear $Z(t)^{-1/2}$ scaling.

Longer regimes of linearly decreasing $Z^{-1/2}$ scaling were previously found during the reconnection of both trefoils (Kerr 2018a) and anti-parallel vortices (Kerr 2018b), with two significant differences. First, their initial configurations do not have coils and second it is $B_\nu(t) = (\sqrt{\nu}Z)^{-1/2}$ that converges, not simply $Z^{-1/2}$. What might be similar is that the $(\sqrt{\nu}Z)^{-1/2}$ scaling does not begin until viscous reconnection begins and some twist develops, determined crudely for the trefoils and seen visually on the reconnected anti-parallel vortices. Could this mean that linear $Z^{-1/2}$ regimes require vortices with twist? Either imposed or generated by viscous reconnection?

4. Summary

The three primary results of this paper are:

- A set of algorithms has been demonstrated that are able to independently extract the

writhe Wr, the twist Tw and the self-linking $\mathcal{L}_S$ numbers of closed trajectories determined from grid-based vector fields. In addition to the Gauss linking algorithms (2.13) for Wr and $\mathcal{L}_S$ (Kerr 2018a), by taking every fourth point on trajectories $\boldsymbol{x}_j(s)$ (2.10), the Frenet-Serret (2.11) twist (2.12) can now be found.

  - ◦ Furthermore, since the experiments are already finding digital trajectories, these direct methods for calculating the topological numbers might be capable of replacing the use of the trajectory crossings (Scheeler *et al.* 2014), with validation provided by $\mathcal{L}_S = Tw + Wr$ (1.1).
  - ◦ The current limitations of using these methods for quantitative analysis, in particular for tightly coiled vortices, are discussed. However, even then, and as configurations become turbulent (Kerr 2018a), they can provide useful qualitative insight.

- For the Scheeler *et al.* (2017) coiled ring experiments, only their $t = 0$ writhe Wr values are confirmed and by applying the twist integral (2.12) to the coil trajectories (2.7) one gets $Tw \gg Wr$, not $Tw \ll Wr$.
  - ◦ Their self-linking $\mathcal{L}_S$ numbers gotten by using $\mathcal{H}_c$ (2.14) for $\mathcal{H}_T$ in (1.2) are also inconsistent with values gotten from using the analytic centreline trajectories (2.7).
  - ◦ The origin of the faulty $\mathcal{L}_S$ values is probably two-fold. First, it is empirically shown that for single coils with a large twist Tw that $\mathcal{H}_c \sim Wr\Gamma^2$ (1.3) with $Wr \ll \mathcal{L}_S$. Not $\mathcal{H}_c \sim \mathcal{L}_S\Gamma^2$ (1.2). Second, there could be errors related to $u_\omega < 0$ in (2.14), as discussed in section 3.3.
- Consistent with the numerical results for reconnecting trefoil vortices and anti-parallel vortices, until the first reconnection is finished, the global helicity $\mathcal{H}$ is preserved and there is linear $Z^{-1/2}(t)$ enstrophy scaling. Comparison of the configurations suggests that twist, either imposed or due to viscous reconnection, could be the common property.

These final results confirm that there is a relationship between the evolution of the topological and the continuum dynamics, with the writhe and twist playing complementary roles, but not as suggested by Scheeler *et al.* (2017). Besides continued analysis of the existing coiled rings, more coiled ring calculations are needed. These should include rings with thinner vortices and a wider range of viscosities. Furthermore, with the new tool for finding the twist and better insight into its role, the trefoil calculations need to be revisited.

Acknowledgements I wish to thank S. Schleimer and M.A. Berger for discussions on topological structures. Computing resources have been provided by the Centre for Scientific Computing at the University of Warwick.

REFERENCES

Berger, M.A., & Field, G.B. 1984 The topological properties of magnetic helicity. *J. Fluid Mech.* **147**, 133-148.

Calugareanu, G. 1959 L'intégral de Gauss et l'analyse des noeuds tridimensionels. *Res. Math. Pures Appl.* **4**, 5–20.

Kerr, R.M. 2013a Swirling, turbulent vortex rings formed from a chain reaction of reconnection events. *Phys. Fluids* **25**, 065101.

Kerr, R.M. 2018 Trefoil knot timescales for reconnection and helicity. *Fluid Dynamics Res.* **50**, 011422.

Kerr, R.M. 2018 Enstrophy and circulation scaling for Navier-Stokes reconnection. *J. Fluid Mech.* **839**, R2.

Kleckner, D., & Irvine, W.T.M 2013 Creation and dynamics of knotted vortices. *Nature Phys.* **9**, 253–258.

Laing, C. E., Ricca, R.L, & Sumners, D.W.L. 2015 Conservation of writhe helicity under anti-parallel reconnection.. *Sci. Rep.* **5**, 9224.

Moffatt, H.K., & Ricca, R. 1992 Helicity and the Calugareanu invariant. *Proc. R. Soc. Long. A* **439**, 411-429.

Pohl, W.F. 1968 The self-linking number of closed space curve. *J. Math. Mech* **17**, 975–985.

Rorai, C., Skipper, J., Kerr, R.M., & Sreenivasan, K.R. 2016 Approach and separation of quantised vortices with balanced cores. *J. Fluid Mech.* **808**, 641–667.

Scheeler, M. W., Kleckner, D., Proment, D., Kindlmann, G. L., & Irvine, W.T.M. 2014 Helicity conservation by flow across scales in reconnecting vortex links and knots. *Proc. Nat. Acac. Sci.* **111**, 15350–15355.

Scheeler, M. W., van Rees, W., Kedia, H., Kleckner, D., & Irvine, W. 2017 Complete measurement of helicity and its dynamics in vortex tubes.. *Science* **357**, 487.